

# Adaptive Hyperspectral Mixed Noise Removal

Tai-Xiang Jiang<sup>✉</sup>, Member, IEEE, Lina Zhuang<sup>✉</sup>, Member, IEEE, Ting-Zhu Huang<sup>✉</sup>, Xi-Le Zhao<sup>✉</sup>, and José M. Bioucas-Dias<sup>✉</sup>, Fellow, IEEE

**Abstract**—This article proposes a new denoising method for hyperspectral images (HSIs) corrupted by mixtures (in a statistical sense) of stripe noise, Gaussian noise, and impulsive noise. The proposed method has three distinctive features: 1) it exploits the intrinsic characteristics of HSIs, namely, low-rank and self-similarity; 2) the observation noise is assumed to be additive and modeled by a mixture of Gaussian (MoG) densities; 3) the inference is performed with an expectation maximization (EM) algorithm, which, in addition to the clean HSI, also estimates the mixture parameters (posterior probability of each mode and variances). Comparisons of the proposed method with state-of-the-art algorithms provide experimental evidence of the effectiveness of the proposed denoising algorithm. A MATLAB demo of this work will be available at <https://github.com/TaiXiangJiang> for the sake of reproducibility.

**Index Terms**—Denoising, expectation maximization (EM), low-rank, mixed noise hyperspectral images (HSIs), mixture of Gaussians, self-similarity.

## I. INTRODUCTION

HYPERSPECTRAL remote sensing images, captured from sensors over hundreds or thousands of spectral bands and containing abundant spatial and spectral knowledge, have been widely used in countless applications (e.g., terrain detection, mineral exploration, pharmaceutical counterfeiting, vegetation, and environmental monitoring), due to its preservation of full-band information under a real scene [1], [2]. However, the hyperspectral images (HSIs) are often unavoidably corrupted by several types of noises, such as Gaussian noise, Poissonian noise, quantization noise, impulse noise, deadlines, and stripes, and these degradations linked with various mechanisms often compromise the potential of HSIs in the subsequent processing, e.g., classification, target detection, and unmixing. Therefore, HSI denoising is an

Manuscript received April 1, 2021; revised May 3, 2021; accepted May 26, 2021. Date of publication June 15, 2021; date of current version January 12, 2022. This work was supported in part by the Fundamental Research Funds for the Central Universities under Grant JBK2102001, in part by the National Natural Science Foundation of China under Grant 12001446, Grant 61772003, Grant 61876203, and Grant 42001287; in part by the Applied Basic Research Project of Sichuan Province under Grant 2021YJ0107, in part by the Key Project of Applied Basic Research in Sichuan Province under Grant 2020YJ0216, in part by the National Key Research; and in part by Development Program of China under Grant 2020YFA0714001. (*Corresponding author: Lina Zhuang*)

Tai-Xiang Jiang is with the School of Economic Information Engineering, Southwestern University of Finance and Economics, Chengdu 611731, China (e-mail: [taixiangjiang@gmail.com](mailto:taixiangjiang@gmail.com)).

Lina Zhuang is with the Department of Mathematics, The University of Hong Kong, Hong Kong, China (e-mail: [linazhuang@qq.com](mailto:linazhuang@qq.com)).

Ting-Zhu Huang and Xi-Le Zhao are with the School of Mathematical Sciences, University of Electronic Science and Technology of China, Chengdu 611731, China (e-mail: [tingzhuhuang@126.com](mailto:tingzhuhuang@126.com); [xlzhao122003@163.com](mailto:xlzhao122003@163.com)).

José M. Bioucas-Dias is with the Instituto de Telecomunicações, Instituto Superior Técnico, Universidade de Lisboa, 1049-001 Lisbon, Portugal (e-mail: [bioucas@lx.it.pt](mailto:bioucas@lx.it.pt)).

Digital Object Identifier 10.1109/TGRS.2021.3085779

essential preprocessing step for improving the performance of subsequent applications.

Large research efforts have been devoted to HSI denoising/restoration [3]–[32]. Among them, two critical points have been taken into consideration. One is that of simultaneously preserving the structure of the clean HSIs and utilizing the inner correlation while denoising. HSIs are strongly correlated in the spectral-spatial domain, implying that they are low-rank, piecewise smooth, and self-similar. Another one is an appropriate modeling strategy for the noise since that the noise often exhibits very complex statistical distributions in many real HSI applications.

The low dimensionality, i.e., the low-rankness, of the clean HSIs is a global property, which stems from the high correlation (redundance) existing among the hyperspectral vectors. This property has been exploited by: 1) representing the spectral vectors in low-dimensional subspaces, FastHyDe [3], RHyDe [4], global local factorization (GLF) [5], HySure [6], HyDroS [7], and NGmeet [8] for example; 2) minimizing the convex/nonconvex surrogate of the matrix/tensor rank function like low-rank matrix recovery (LRMR) [9], SpaLr [10], noise-adjusted iterative low-rank matrix approximation (NAILRMA) [11], structure tensor total variation-regularized weighted nuclear norm minimization (STWNNM) [12], low-rank tensor recovery (LRTR) [14], weighted Schatten p-norm (WSN)-low-rank matrix approximation (LRMA) [15], framelet based tensor-singular value decomposition (F-TSVD) [16], and NonLRMA [17]; 3) matrix/tensor factorization such as multitask sparse nonnegative matrix factorization (MTSNMF) [18], R-Co nonnegative matrix factorization (NMF) [33], total variation-regularized low-rank matrix factorization (LRTV) [19], fast low-rank tensor completion (F-LRTC) [20], NMoG [21], total variation regularized low-rank tensor decomposition (LRTDTV) [22], nonlocal tensor-ring decomposition (NLTR) [23], and double low-rank matrix decomposition (DLRD) [24]. In the meantime, the widespread piecewise smoothness, a local property throughout the spatial and spectral domain, has also been widely exploited, for example, via total-variation regularizations (see, e.g., [6], [12], [19], [22], [24]–[27], [31]).

Over the past decade, the image self-similarity, a nonlocal property, underlies the state of the art denoising in single-band natural images. This form of prior, or regularizer, has been fully exploited in nonlocal means [34], BM3D [35], nonlocally centralized sparse representation (NCSR) [36], low-rank regularized collaborative filtering (LRCF) [37], expected patch Log Likelihood method (EPLL) [38], Gaussian mixture model (GMM) [39], and weighted nuclear norm minimization (WNNM) [40]. These ideas have been extended to color images [41]–[43], ultrasound images [44], volumetric images [45], videos [46], and to multispectral/HSIs [29]–[32], [47],

[48]. Meanwhile, the presence of the deep-learning-based method, with improved modeling capacity, brings in another category of the current most effective image denoising methods, from the gray-scale (or color) image denoising [49]–[54] to the HSI denoising [55]–[57]. As concluded in [58], the nonlocal methods result in superior noise removal where the image exhibits strong self-similarity, such on edges or on regular texture, but yield inferior performance on pseudorandom textures or singular features, while convolutional neural network (CNN)-based methods maintain the ability to learn and extract complex image features but yield inferior performance on regular textures with high self-similarity. Ongoing efforts are made to simultaneously utilize their advantages [58]–[60].

Zhuang *et al.* proposed a cascade of methods (FastHyDe [3], RHyDe [4] and GLF [5]), which tactfully and compactly exploit HSIs' low-rankness and self-similarity with very low computational complexity. These methods, in this research line, start by identifying the subspace where the spectral vectors live from the observed HSIs [61], and then formulate the denoising problem with respect to (w.r.t.) the representation coefficients in the subspace. Instead of investing efforts in tailoring regularizers to address the representation coefficients denoising problem, Zhuang *et al.* directly use the BM3D [35] denoiser within the plug-and-play (PnP) prior framework [62]–[64]. The formulation of the denoising problem w.r.t. the representation coefficients opens a door for the HSI denoising to expediently use off-the-shelf denoising algorithms designed for natural gray level images with good preservation of the inner structure. At the same time, the alternative Poissonian noise, becoming the main concern in real HSIs [65]–[67] on account of the fact that, in the new generation hyperspectral sensors, each spectral channel receives fewer photons due to the increase in the number of spectral bands and the decrease in the spectral bandwidth, is handled by Zhuang *et al.* via being converted into approximately additive Gaussian noise with nearly constant variance using variance-stabilizing transformations [68].

Although FastHyDe [3] and GLF [5] achieved unexceptionable results for the task of either Gaussian or Poissonian noise removal, they are not robust to the mixed noise (*e.g.*, Gaussian & stripe noise or Poissonian & impulsive noise). HyDRoS [7] is robust to the dead pixels after decomposing the noise into a Gaussian term plus a sparse term and imposing the  $\ell_1$  regularization on the latter term. Many methods (see, *e.g.*, LRMR [9], NonLRMA [17], LRTV [19], and LRTR [14] assume the noise is Gaussian & sparse and adopt: 1) the sparsity inducing  $\ell_1$  or  $\ell_{2,1}$  norm regularization terms to regularize the sparse component; 2) the Frobenius norm fidelity term, accounting for the independent and identically distributed (i.i.d.) Gaussian noise, to rectify the deviation between the reconstruction and the observed HSI. As mentioned before, in many real applications, the noise often exhibits very complex statistical distributions. This motivates us to consider a more flexible modeling strategy to tackle such complex noise cases.

#### A. Contribution

We propose an **adaptive hyperspectral image denoising** method (termed *AdHyDe*) by modeling the complex noise

as an additive term with a MoG densities, which is a universal approximation to any continuous distribution and hence capable of modeling a wider range of noise distributions [69]. To automatically estimate the parameters involved in different noise distributions, we design an expectation maximization (EM) algorithm. Following the research line in [3]–[5], our method takes full advantage of the spectral low dimension and spatial self-similarity<sup>1</sup> of the HSIs.

This work is an extension of the material published in [70]. The new material is the following: 1) AdHyDe is herein introduced and characterized in more detail; 2) a neural network denoiser, the a fast and flexible denoising convolutional neural network (FFDNet) [53], is seamlessly embedded within our algorithm; and 3) exhaustive array of experiments and comparisons are carried out.

The outline of this article is given as follows. Section II introduces the main results, consisting of the problem formulation in Section II-A and the proposed EM algorithm in Section II-B Experimental results including comparisons with the state of the art are reported in Section III. Finally, we draw some conclusions in Section IV.

## II. MAIN RESULTS

Let  $\mathbf{Y} \in \mathbb{R}^{b \times n}$  denote an observed HSI with  $n$  spectral pixels of size  $b$  (spectral bands). The noise is assumed to be additive. Therefore, we may write

$$\mathbf{Y} = \mathbf{X} + \mathbf{N} \quad (1)$$

where  $\mathbf{X}$  and  $\mathbf{N} \in \mathbb{R}^{b \times n}$  are, respectively, the clean HSI and the noise.

Since, with a very good approximation, we are assuming that the spectral vectors (columns of  $\mathbf{X}$ ) live in a  $s$ -dimensional subspace [1], [3], we may write

$$\mathbf{Y} = \mathbf{E}\mathbf{Z} + \mathbf{N} \quad (2)$$

where columns of  $\mathbf{E} \in \mathbb{R}^{b \times s}$  (with  $s \ll b$ ) span the subspace and  $\mathbf{Z} \in \mathbb{R}^{s \times n}$  represents the coefficients for  $\mathbf{X}$  w.r.t.  $\mathbf{E}$ . Matrix  $\mathbf{E}$ , assumed to be semiunitary (*i.e.*,  $\mathbf{E}^\top \mathbf{E} = \mathbf{I}_s$  with  $\mathbf{I}_s$  indicating the identity matrix of dimension  $s$ ), spans an orthogonal subspace. The subspace is estimated with, for example, the HySime algorithm [61] or singular value decomposition (SVD) of  $\mathbf{Y}$  in the case when the noise is i.i.d. Matrix  $\mathbf{Z}$  contains the representation coefficients of  $\mathbf{X}$  w.r.t.  $\mathbf{E}$  and the images associated with its rows are termed as *eigenimages* [3]. As widely discussed in [3], [7], and [20], the eigenimages are linear combinations of the bands of  $\mathbf{X}$ , which represent the reflectance of the same surface at different wavelengths, and thereof maintain the spatial structures, such as piecewise smoothness and the nonlocal similarity. Hence the denoising methods which utilize the piecewise smoothness and the nonlocal similarity can be directly applied to the eigenimages. Moreover, formulating the denoising problem w.r.t. the representation coefficients has been validated effective [3]–[5], [7] and well preserves the spectral correlation of the HSI with less computation.

<sup>1</sup>When plugging and playing the CNN denoisers, it is believed to exploit the data-driven prior.

### A. Problem Formulation

Using the Bayes rule, the posterior probability distribution of  $\mathbf{Z}$  conditioned to  $\mathbf{Y}$  is given by

$$p(\mathbf{Z}|\mathbf{Y}) = \frac{p(\mathbf{Y}|\mathbf{Z})p(\mathbf{Z})}{p(\mathbf{Y})} \quad (3)$$

where  $p(\mathbf{Y}|\mathbf{Z})$  is the probability of  $\mathbf{Y}$  given  $\mathbf{Z}$  (the *likelihood function*) and  $p(\mathbf{Z})$  is *a priori* probability density function of  $\mathbf{Z}$ . The *maximum a posteriori* (MAP) estimate of  $\mathbf{Z}$  is

$$\hat{\mathbf{Z}} \in \arg \max_{\mathbf{Z}} \log p(\mathbf{Z}|\mathbf{Y}) = \arg \max_{\mathbf{Z}} \log p(\mathbf{Y}|\mathbf{Z}) + \log p(\mathbf{Z}). \quad (4)$$

In this article, we consider that the noise is an MoG mixture with only two modes: the first mode models the band-wise i.i.d. zero-mean white Gaussian noise with variance  $\sigma_{i,1}^2$  for the  $i$ th band. The second term models stripe and impulsive noise in the  $i$ th band and it is assumed to follow a Gaussian distribution with zero-mean and a very large variance  $\sigma_{i,2}^2$  ( $\sigma_{i,2}^2 \gg \sigma_{i,1}^2$ ). Hence

$$p(y_{ij}|x_{ij}) = \sum_{k=1}^2 \alpha_{i,k} \mathcal{N}(y_{ij} - x_{ij}, \sigma_{i,k}^2) \quad (5)$$

where  $y_{ij} := [\mathbf{Y}]_{ij}$ ,  $x_{ij} := [\mathbf{EZ}]_{ij}$ ,  $\alpha_{i,k} \geq 0$  is the probability of mode  $k \in \{1, 2\}$  in the  $i$ th band, and  $\mathcal{N}(y - \mu, \sigma^2)$  denotes a Gaussian density with mean  $\mu$  and variance  $\sigma^2$  computed at  $y$ .

Assuming that  $\mathbf{Z}$  and  $\mathbf{N}$  are independent, it follows:

$$p(\mathbf{Y}|\mathbf{Z}) = \prod_{i=1}^b \prod_{j=1}^n p(y_{ij}|x_{ij}). \quad (6)$$

Then, the MAP problem (4) turns out to be

$$\widehat{\Theta} \in \arg \max_{\Theta} \left\{ \prod_{i=1}^b \prod_{j=1}^n \left( \sum_{k=1}^2 \alpha_{i,k} \mathcal{N}(y_{ij} - x_{ij}, \sigma_{i,k}^2) \right) p(\mathbf{Z}) \right\} \quad (7)$$

where  $\Theta := \{\mathbf{Z}, \alpha_k, \sigma_{i,k}^2\}$  ( $i = 1, \dots, b$  and  $k = 1, 2$ ).

### B. Proposed EM Algorithm

Problem (7) is nonconvex and we use the EM algorithm [71] to compute a local optima. To apply the EM algorithm, as usual in mixtures, we introduce the latent variables  $u_{ijk}$  (playing the role of missing data), for  $ijk \in \{1, \dots, b\} \times \{1, \dots, n\} \times \{1, 2\}$ , which select the active mode at band  $i$  and pixel  $j$ .

Let  $\Theta^{(t)} := \{\mathbf{Z}^{(t)}, \alpha_{i,k}^{(t)}, (\sigma_{i,k}^2)^{(t)}\}$  ( $i = 1, \dots, b$  and  $k = 1, 2$ ) denote the set of parameters at the  $t$ th iteration of the EM algorithm. Then, the E-step and the M-step amount to compute (see [71] for details)

1) *E-Step*: The posterior responsibility of mixture  $k$  ( $= 1, 2$ ) for generating the noise of  $y_{ij}$  ( $i = 1, 2, \dots, b$ ,  $j = 1, 2, \dots, n$ ) is calculated by

$$\omega_{i,j,k}^t = \mathbb{E}[u_{i,j,k}|\mathbf{Y}, \Theta^{(t)}] = \frac{\alpha_{i,k}^t \mathcal{N}(y_{ij} - x_{ij}^{(t)}, (\sigma_{i,k}^2)^{(t)})}{\sum_{p=1}^2 \alpha_{i,p}^t \mathcal{N}(y_{ij} - x_{ij}^{(t)}, (\sigma_{i,p}^2)^{(t)})}. \quad (8)$$

2) *M-Step*: Construct the so-called  $Q$  function:

$$\begin{aligned} Q(\Theta, \Theta^{(t)}) &= \sum_{i=1}^b \sum_{j=1}^n \sum_{k=1}^2 \omega_{i,j,k}^t \\ &\times \left( -\frac{1}{2} \log(2\pi\sigma_{i,k}^2) - \frac{(y_{ij} - x_{ij})^2}{2\sigma_{i,k}^2} + \log \alpha_{i,k} \right) + \log p(\mathbf{Z}). \end{aligned} \quad (9)$$

Then, optimize  $Q(\Theta, \Theta^{(t)})$  w.r.t.  $\Theta$ . The optimization w.r.t.  $\alpha_{i,k}$ ,  $\sigma_{i,k}$ , for  $k = 1, 2$  and  $i = 1, \dots, b$ , yields

$$\alpha_{i,k} = \frac{\sum_j \omega_{i,j,k}^t}{\sum_{j,p} \omega_{i,j,p}^t}, \quad \sigma_{i,k}^2 = \frac{\sum_j \omega_{i,j,k}^t (y_{ij} - x_{ij})^2}{\sum_j \omega_{i,j,k}^t}. \quad (10)$$

We remark that  $\alpha_{i,2} = 1 - \alpha_{i,1}$ . The optimization w.r.t.  $\mathbf{Z}$  is (recall that  $x_{ij} = [\mathbf{EZ}]_{ij}$ )

$$\min_{\mathbf{Z}} \sum_{i=1}^b \sum_{j=1}^n \sum_{k=1}^2 \omega_{i,j,k}^t \left( \frac{(y_{ij} - x_{ij})^2}{2\sigma_{i,k}^2} \right) - \log p(\mathbf{Z}). \quad (11)$$

Optimization (11) may be compactly written as

$$\min_{\mathbf{Z}} \sum_{k=1}^2 \frac{1}{2} \|\mathbf{M}_k \odot (\mathbf{Y} - \mathbf{EZ})\|_F^2 + \log p(\mathbf{Z}) \quad (12)$$

where  $[\mathbf{M}_k]_{i,j} := (\omega_{i,j,k}^t / \sigma_{i,k}^2)^{1/2}$ ,  $\|\mathbf{X}\|_F^2 := (\text{trace}(\mathbf{XX}^\top))^{1/2}$ , and  $\odot$  stands for element-wise multiplication. Considering that  $\sigma_{i,2} \gg \sigma_{i,1}$ , optimization (12) is well approximated by

$$\min_{\mathbf{Z}} \frac{1}{2} \|\mathbf{M}_1 \odot (\mathbf{Y} - \mathbf{EZ})\|_F^2 + \lambda \phi(\mathbf{Z}) \quad (13)$$

where  $\lambda \phi(\mathbf{Z}) := -\log p(\mathbf{Z})$  and  $\lambda > 0$  acts as a regularization parameter. We note that (13) is a convex problem, provided that  $\phi$  is convex. We use split augmented Lagrangian shrinkage algorithm (SALSA) [72] to solve (13). To set the stage for SALSA, we start by reformulating (13) as the equivalent constrained optimization

$$\begin{aligned} \min_{\mathbf{Z}} \frac{1}{2} \|\mathbf{M}_1 \odot (\mathbf{Y} - \mathbf{V}_1)\|_F^2 + \lambda \phi(\mathbf{V}_2) \\ \text{s.t. } \mathbf{V}_1 = \mathbf{EZ}, \quad \mathbf{V}_2 = \mathbf{Z}. \end{aligned} \quad (14)$$

The augmented Lagrangian function for (14) is

$$\begin{aligned} L(\mathbf{Z}, \mathbf{V}_1, \mathbf{V}_2, \mathbf{D}_1, \mathbf{D}_2) &= \frac{1}{2} \|\mathbf{M}_1 \odot (\mathbf{Y} - \mathbf{V}_1)\|_F^2 + \lambda \phi(\mathbf{V}_2) \\ &+ \frac{\mu}{2} \|\mathbf{EZ} - \mathbf{V}_1 - \mathbf{D}_1\|_F^2 + \frac{\mu}{2} \|\mathbf{Z} - \mathbf{V}_2 - \mathbf{D}_2\|_F^2 \end{aligned} \quad (15)$$

where  $\mathbf{D}_1, \mathbf{D}_2$  are scaled Lagrangian multipliers and  $\mu > 0$ . Then SALSA iteratively optimize (15) w.r.t.  $\mathbf{Z}, \mathbf{V}_1, \mathbf{V}_2$  and

update  $\mathbf{D}_1, \mathbf{D}_2$ , leading to the following updates:

$$\left\{ \begin{array}{l} \mathbf{Z}^{(p+1)} = \frac{1}{2} \left( \mathbf{E}^\top (\mathbf{V}_1^{(p)} + \mathbf{D}_1^{(p)}) + \mathbf{D}_2^{(p)} + \mathbf{V}_2^{(p)} \right) \\ \mathbf{V}_1^{(p+1)} = \left( \mathbf{E}\mathbf{Z}^{(p+1)} - \mathbf{D}_1^{(p)} + \mathbf{M}_1 \odot \mathbf{M}_1 \odot \mathbf{Y} \right) \\ \quad \oslash (\mathbf{M}_1 \odot \mathbf{M}_1 \oplus \mu) \\ \mathbf{V}_2^{(p+1)} = \arg \min_{\mathbf{V}_2} \frac{\mu}{2} \left\| \mathbf{Z}^{(p+1)} - \mathbf{V}_2 - \mathbf{D}_2^{(p)} \right\|_F^2 \\ \quad + \lambda \phi(\mathbf{V}_2) \\ \mathbf{D}_1^{(p+1)} = \mathbf{D}_1^{(p)} - \left( \mathbf{E}\mathbf{Z}^{(p+1)} - \mathbf{V}_1^{(p+1)} \right) \\ \mathbf{D}_2^{(p+1)} = \mathbf{D}_2^{(p)} - \left( \mathbf{Z}^{(p+1)} - \mathbf{V}_2^{(p+1)} \right) \end{array} \right. \quad (16)$$

where the superscript  $.^{(p)}$  represents the time evolution step of the SALSA iterations.

To solve the  $\mathbf{V}_2$  subproblem, we resort to the plug-and-play (PnP) prior framework [62], [73]. Considering the rows of  $\mathbf{Z}$  tend to be decorrelated [3], we assume that the function  $\phi$  is decoupled w.r.t. the rows of  $\mathbf{V}_2$ , that is,

$$\phi(\mathbf{V}_2) = \sum_{i=1}^s \phi(\mathbf{V}_2^i) \quad (17)$$

where  $\mathbf{V}_2^i \in \mathbb{R}^{1 \times n}$  is the  $i$ th row of  $\mathbf{V}_2$ . Under this hypothesis, the solution of the  $\mathbf{V}_2$  subproblem is decoupled w.r.t.  $\mathbf{V}_2^i$  and may be written as

$$\begin{aligned} \mathbf{V}_2^{(p+1)} &= \psi_{\frac{\lambda}{\mu} \phi} \left( \mathbf{Z}^{(p+1)} - \mathbf{D}_2^{(p)} \right) \\ &= \begin{bmatrix} \psi_{\frac{\lambda}{\mu} \phi_1} \left( \mathbf{Z}^{1(p+1)} - \mathbf{D}_2^{1(p)} \right) \\ \psi_{\frac{\lambda}{\mu} \phi_2} \left( \mathbf{Z}^{2(p+1)} - \mathbf{D}_2^{2(p)} \right) \\ \vdots \\ \psi_{\frac{\lambda}{\mu} \phi_s} \left( \mathbf{Z}^{s(p+1)} - \mathbf{D}_2^{s(p)} \right) \end{bmatrix} \end{aligned} \quad (18)$$

where

$$\psi_{\frac{\lambda}{\mu} \phi_i}(\mathbf{y}) = \arg \min_w \frac{\mu}{2} \|\mathbf{y} - \mathbf{w}\|_F^2 + \lambda \phi_i(\mathbf{w}) \quad (19)$$

is the so-called denoising operator or Moreau proximity operator of  $\phi_i$  [74].

In this article, we not only use BM3D, a very fast state-of-the-art denoiser conceived to enforce self-similarity, as in [3] but also herein adopt the CNN-based denoiser FFDNet [53], which has been pretrained in MATLAB (R2015b) environment with MatConvNet package [75] and an Nvidia Titan X Pascal GPU by the authors of [53] and provides a flexible way to handle various types of noise with a single network. As BM3D and FFDNet are single-band image denoisers, thus each vector  $(\mathbf{Z}^{l(p+1)} - \mathbf{D}_2^{l(p)})$  ( $l = 1, 2, \dots, s$ ) needs to be folded back to an image form for processing. Since that both BM3D and FFDNet need an input estimation of the noise level, which plays the role of controlling the tradeoff between noise reduction and detail preservation, we need to determine the noise level of each  $\mathbf{Z}^{l(p+1)} - \mathbf{D}_2^{l(p)}$  ( $l = 1, 2, \dots, s$ ). It is notable that only the Gaussian noise needs to be taken into consideration when solving optimization problem (12) because our strategy

is to ignore the item  $(1/2)\|\mathbf{M}_2 \odot (\mathbf{Y} - \mathbf{EZ})\|_F^2$  considering  $\sigma_{i,2} \gg \sigma_{i,1}$  and  $[\mathbf{M}_2]_{i,j} = (\omega_{ij,2}^t / \sigma_{i,2}^2)^{1/2} \ll [\mathbf{M}_1]_{i,j} = (\omega_{ij,1}^t / \sigma_{i,1}^2)^{1/2}$ . As the first and second components in the MoG mixture are, respectively, corresponding to Gaussian noise and non-Gaussian noise, the data term  $(1/2)\|\mathbf{M}_1 \odot (\mathbf{Y} - \mathbf{EZ})\|_F^2$  in our objective function (13) only measures the discrepancy between observations corrupted by Gaussian noise and the underlying clean image. In other words, the data term in (13) accounts for Gaussian noise, thus the setting of regularization parameter  $\lambda$  is related to Gaussian noise level, which need to be estimated. Another noteworthy fact is that the scaled Lagrange multiplier  $\mathbf{D}_2$  tends to be 0 as the SALSA iteration goes on. Hence, we turn to estimate the noise level of  $\mathbf{Z}^{l(p+1)}$ s ( $l = 1, 2, \dots, s$ ).

Supposing that in (1) the noise term can be decomposed into two part, the Gaussian part  $\mathbf{N}_G$  and the non-Gaussian part  $\mathbf{N}_{\text{non-}G}$ , i.e.,  $\mathbf{N} = \mathbf{N}_G + \mathbf{N}_{\text{non-}G}$ . The Gaussian component  $\mathbf{N}_G$  is zeromean, additive, Gaussian, pixelwise independent with spectral covariance  $\mathbf{C} = \mathbb{E}[\mathbf{n}_G \mathbf{n}_G^\top]$ , where  $\mathbf{n}_G$  is a generic column of  $\mathbf{N}_G$ . Considering that the noise variance of the Gaussian noise in each band are estimated in (10), therefore the spectral covariance matrix  $\mathbf{C}$  is diagonal with  $\sigma_{i,1}^2$ s, i.e.,  $\mathbf{C} = \text{diag}(\sigma_{1,1}^2, \sigma_{2,1}^2, \dots, \sigma_{b,1}^2)$ . Thus, after being projected onto the subspace, the covariance matrix of the Gaussian noise w.r.t. the eigenimages can be computed by

$$\begin{aligned} \mathbf{C}_\mathbf{Z} &= \mathbb{E}[\mathbf{E}^\top \mathbf{n}_G \mathbf{n}_G^\top \mathbf{E}] = \mathbf{E}^\top \mathbb{E}[\mathbf{n}_G \mathbf{n}_G^\top] \mathbf{E} = \mathbf{E}^\top \mathbf{C} \mathbf{E} \\ &= \text{diag}(\mathbf{e}_1^\top \mathbf{C} \mathbf{e}_1, \mathbf{e}_2^\top \mathbf{C} \mathbf{e}_2, \dots, \mathbf{e}_s^\top \mathbf{C} \mathbf{e}_s) \end{aligned} \quad (20)$$

where  $\mathbb{E}$  indicates computing the expectation and  $\mathbf{e}_l$  ( $l = 1, 2, \dots, s$ ) denotes the  $l$ th column of  $\mathbf{E}$ .

A pertinent question when utilizing the PnP framework is that, given a denoiser, whether there exists a convex regularizer of which the denoiser is the proximity operator. The answer for BM3D, LRCF, and GMM is negative [76], as it is for most state-of-the-art denoisers. However, this fact should not prevent us to use such denoisers, as they have been successfully plugged and played to solve a number of inverse problems [3], [4], [76]. In this work, we selected BM3D, as it is the state-of-the-art and a very fast implementation thereof is publicly available.

3) *Preprocessing*: The EM algorithm is initialized with  $\Theta^{(0)} = \{\mathbf{Z}^{(0)}, \alpha_k^{(0)}, (\sigma_{i,k}^2)^{(0)}\}$ , where  $\mathbf{Z}^{(0)} = \mathbf{E}^\top \tilde{\mathbf{Y}}$  and  $\tilde{\mathbf{Y}}$  is obtained by bandwise prefiltering the noisy HSI with a  $3 \times 3$  median filter,  $\alpha_k^{(0)}$  and  $(\sigma_k^2)^{(0)}$  given by (10)

$$\omega_{ij,1}^{(0)} = \begin{cases} 1, & \text{if } |\tilde{x}_{ij} - y_{ij}| < 3\hat{\sigma}_{i,1} \\ 0, & \text{otherwise,} \end{cases} \quad \omega_{ij,2}^{(0)} = 1 - \omega_{ij,1}^{(0)} \quad (21)$$

with  $\tilde{\mathbf{X}} = \mathbf{E}\mathbf{Z}^{(0)}$ ,  $\tilde{x}_{ij} := [\tilde{\mathbf{X}}]_{ij}$ , and  $\hat{\sigma}_{i,1}$  given by the sample variance of the vector  $(\tilde{\mathbf{Y}}(i,:) - \tilde{\mathbf{X}}(i,:))$ .

Algorithm 1 shows the pseudocode for the proposed HSI denoising method. Given an HSI of the size  $b \times n$  with subspace dimension  $k$  ( $k \ll d$ ), the computation complexity of updating  $\omega_{ij,k}^{(t)}$  in the E-step is  $\mathcal{O}(nb)$ . For the M-step, updating  $\alpha_{i,k}^{(t)}$  and  $(\sigma_{i,k}^2)^{(t)}$  costs  $\mathcal{O}(nb)$  and each single SALSA iteration costs  $\mathcal{O}(2nkb + bn + kd) = \mathcal{O}(nkb + kd)$ , where  $d$  represents the computational complexity of denoising an eigenimage.

TABLE I  
QUANTITATIVE ASSESSMENTS OF ALL COMPETING METHODS ON THE DATA PAVIA CITY CENTER AND WASHITON.  
THE BEST TWO REUSLTS ARE HIGHLIGHTED IN RED AND BLUE COLORS, RESPECTIVELY

Data	Noise case	Index	Noisy HSI	BM4D [46]	TDL [48]	SSTV [26]	LRTF-DFR [13]	LRMR [9]	NMoG [21]	LLRGTV [25]	Adhyde (FFDNet)	Adhyde (BM3D)
Pavia City Center	Case 1	MPSNR	14.650	27,223	31,331	35,026	32,242	35,162	37,037	34,697	<b>38.875</b>	<b>38.795</b>
		MSSIM	0.24570	0.75125	0.90050	0.94702	0.89415	0.95437	0.96592	0.96207	<b>0.97905</b>	<b>0.97847</b>
		MIUQI	0.25251	0.75699	0.89992	0.94903	0.90575	0.95371	0.96666	0.96019	<b>0.97881</b>	<b>0.97824</b>
		MSAD	0.67309	0.18429	0.07309	0.07499	0.12662	0.07090	0.05321	0.05748	<b>0.04122</b>	<b>0.04075</b>
		MGMDS	0.18816	0.06626	0.03644	0.01638	0.0244	0.01954	0.00976	0.01919	<b>0.00688</b>	<b>0.00689</b>
	Case 2	time (s)	—	95	<b>9</b>	102	39	39	47	105	<b>4</b>	90
		MPSNR	19.993	28,715	21,953	34,825	33,083	33,333	37,265	34,758	<b>39.083</b>	<b>39.020</b>
		MSSIM	0.47430	0.78918	0.55252	0.94728	0.88308	0.93776	0.96617	0.96284	<b>0.97990</b>	<b>0.97938</b>
		MIUQI	0.51133	0.78613	0.58111	0.94852	0.88524	0.93652	0.96664	0.96070	<b>0.97943</b>	<b>0.97882</b>
		MSAD	0.56487	0.43627	0.54460	0.07893	0.29693	0.11712	0.05250	0.05772	<b>0.04044</b>	<b>0.03993</b>
	Case 3	MGMDS	0.13315	0.08634	0.11844	0.01776	0.04024	0.03522	0.00900	0.01875	<b>0.00670</b>	<b>0.00668</b>
		time (s)	—	96	<b>15</b>	103	40	39	63	106	<b>10</b>	262
		MPSNR	13.605	23,933	25,754	34,077	32,251	32,733	36,650	34,169	<b>38.772</b>	<b>38.590</b>
		MSSIM	0.21528	0.64424	0.69686	0.93670	0.87297	0.92648	0.96153	0.95727	<b>0.97859</b>	<b>0.97713</b>
		MIUQI	0.22260	0.64576	0.70507	0.93865	0.87849	0.92594	0.96230	0.95482	<b>0.97806</b>	<b>0.97650</b>
	Case 4	MSAD	0.76061	0.41565	0.47748	0.08643	0.30866	0.12522	0.05664	0.06306	<b>0.04078</b>	<b>0.04123</b>
		MGMDS	0.20844	0.12065	0.09605	0.02024	0.03917	0.03674	0.01033	0.02207	<b>0.00729</b>	<b>0.00731</b>
		time (s)	—	107	<b>14</b>	110	42	38	68	106	<b>10</b>	253
		MPSNR	10.620	21,094	22,925	34,832	33,115	31,124	36,327	35,124	<b>40.192</b>	<b>39.253</b>
		MSSIM	0.14830	0.54199	0.66361	0.94938	0.91861	0.87975	0.93885	0.95789	<b>0.97370</b>	<b>0.97221</b>
Washington DC Mall	Case 1	MIUQI	0.14973	0.60261	0.70496	0.96642	0.91535	0.90016	0.95288	0.96988	<b>0.98425</b>	<b>0.98265</b>
		MSAD	0.73932	0.46756	0.50586	0.09002	0.12365	0.25417	0.21253	0.07204	<b>0.03658</b>	<b>0.06830</b>
		MGMDS	0.25933	0.18232	0.14376	0.06186	0.04155	0.09999	0.04647	0.06165	<b>0.03589</b>	<b>0.03759</b>
		time (s)	—	96	<b>13</b>	105	42	38	74	108	<b>10</b>	249
		MPSNR	11.975	26,189	28,276	34,511	39,002	35,942	38,333	37,934	<b>40.459</b>	<b>40,343</b>
	Case 2	MSSIM	0.17205	0.71126	0.84033	0.94495	0.98074	0.96305	0.97498	0.97481	<b>0.98502</b>	<b>0.98427</b>
		MIUQI	0.17951	0.68176	0.81968	0.93745	0.97642	0.95497	0.96859	0.96787	<b>0.97987</b>	<b>0.97897</b>
		MSAD	0.83217	0.19657	0.13144	0.08761	0.03843	0.07045	0.05183	0.04929	<b>0.03678</b>	<b>0.03770</b>
		MGMDS	0.23360	0.09605	0.06372	0.02150	0.00725	0.02195	0.00967	0.00973	<b>0.00583</b>	<b>0.00598</b>
		time (s)	—	393	<b>38</b>	416	89	186	141	437	<b>12</b>	289
Washington DC Mall	Case 3	MPSNR	19.527	26,863	22,834	34,105	39,036	33,896	38,741	34,346	<b>40.703</b>	<b>40,625</b>
		MSSIM	0.50049	0.76951	0.60425	0.94528	0.98131	0.95490	0.97632	0.96375	<b>0.98551</b>	<b>0.98485</b>
		MIUQI	0.51863	0.75289	0.61124	0.93732	0.97703	0.94567	0.97006	0.95406	<b>0.98048</b>	<b>0.97968</b>
		MSAD	0.59642	0.48843	0.57247	0.09427	0.03893	0.11113	0.04966	0.07227	<b>0.03597</b>	<b>0.03667</b>
		MGMDS	0.15090	0.10880	0.12989	0.02426	0.00711	0.03490	0.00839	0.02597	<b>0.00559</b>	<b>0.00569</b>
	Case 4	time (s)	—	395	<b>65</b>	415	89	187	200	408	<b>32</b>	491
		MPSNR	11.239	22,864	24,528	33,384	38,736	33,193	38,058	33,960	<b>40.152</b>	<b>40,016</b>
		MSSIM	0.15308	0.61077	0.68674	0.93541	0.97989	0.94780	0.97302	0.95929	<b>0.98419</b>	<b>0.98331</b>
		MIUQI	0.16095	0.58227	0.68034	0.92791	0.97540	0.93864	0.96660	0.94890	<b>0.97899</b>	<b>0.97792</b>
		MSAD	0.87936	0.37421	0.38009	0.10133	0.04032	0.10995	0.05372	0.07492	<b>0.03772</b>	<b>0.03917</b>
	Case 4	MGMDS	0.24685	0.14524	0.11224	0.02740	0.0078	0.03622	0.00938	0.02692	<b>0.00613</b>	<b>0.00634</b>
		time (s)	—	395	<b>61</b>	418	89	186	189	408	<b>31</b>	436
		MPSNR	7.616	19,356	20,401	30,516	36,870	29,843	36,585	32,011	<b>37.502</b>	<b>37,349</b>
		MSSIM	0.07635	0.52895	0.69296	0.89664	<b>0.96942</b>	0.90631	0.94620	0.92881	<b>0.96517</b>	<b>0.96346</b>
		MIUQI	0.08282	0.58108	0.72992	0.91781	0.96262	0.91993	0.95916	0.93985	<b>0.97336</b>	<b>0.97229</b>
		MSAD	0.83435	0.40261	0.28501	0.11835	0.07823	0.17076	0.05863	0.10983	<b>0.05636</b>	<b>0.04992</b>
		MGMDS	0.28968	0.20447	0.15460	0.09731	<b>0.01512</b>	0.10085	0.05706	0.09138	<b>0.04972</b>	<b>0.04992</b>
		time (s)	—	397	<b>48</b>	419	89	192	204	414	<b>30</b>	431

### Algorithm 1 EM Algorithm for HSI Denoising

**Input:**  $\mathbf{Y} \in \mathbb{R}^{b \times n}$   
**Preprocessing:**  $\tilde{\mathbf{Y}} = \text{med}(\mathbf{Y})$ ;  $\mathbf{E} = \text{HySime}(\tilde{\mathbf{Y}})$ ; set  $\omega_{ij,k}^{(0)}$ ,  $\alpha_k^{(0)}$ ,  $(\sigma_{i,k}^2)^{(0)}$  using (21) and (10).  
**1:** repeat  
**2:**     (E-step):  
**3:**         Update  $\omega_{ij,k}^{(t)}$  via (8)  
**4:**     (M-step):  
**5:**         Update  $\alpha_{i,k}^{(t)}$  and  $(\sigma_{i,k}^2)^{(t)}$  via (10)  
**6:**     Update  $\mathbf{Z}^{(t)}$  by running a number of SALSA  
**7:**     iterations (16)  
**8:**      $\mathbf{X}^{(t)} = \mathbf{EZ}^{(t)}$   
**9:** until converge;  
**Output:** The denoised HSI  $\mathbf{X}$

### III. EXPERIMENTS

In this section, to evaluate the performance of the proposed adaptive HIS denoising method (denoted as *AdHyDe*), experiments on both simulated and real data were conducted. Seven

state-of-the-art (hyperspectral) denoising methods, including the method to enhance the self-similarity of nonlocal cubes (BM4D) [46], a nonlocal tensor dictionary learning approach (TDL) [48], spatio-spectral total variation (SSTV) [26], which utilizes the spectral-spatia local continuity, double-factor regularized low-rank tensor factorization (LRTF-DFR) [13], a newly proposed method based on low-rank tensor factorization, LRMR [9], a LRMR algorithm, NMog [21], which models the noise as MoG, and the spatial-spectral total variation regularized local LRMR method (LLRGTV) [25], are selected for the comparison. All experiments were implemented in MATLAB R2017b on a PC with a 3.3-GHz CPU (Intel i5-4590), 16-GB RAM and an Nvidia GTX1080 GPU.

#### A. Evaluation With Simulated Data

In this section, two HSIs, i.e., a subimage of Washington dc Mall dataset<sup>2</sup> (of size 256 rows  $\times$  256 columns  $\times$  191 bands)

<sup>2</sup>This dataset is available from the Purdue University Research Repository (<https://engineering.purdue.edu/biehl/MultiSpec/hyperspectral.html>).

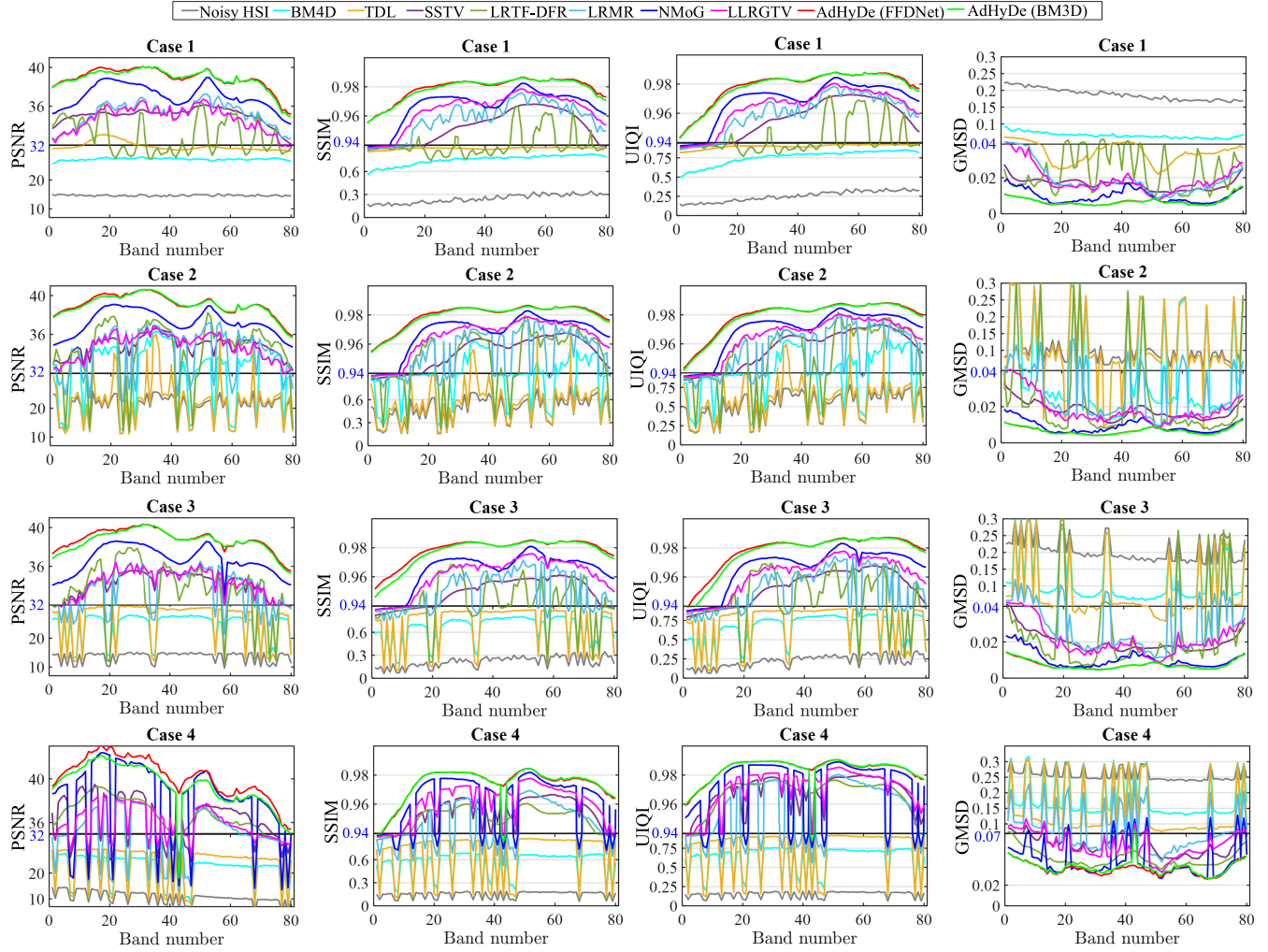


Fig. 1. PSNR, SSIM, UIQI, and GMSD values of each band in the experiments on the Pavia city center dataset in different noise cases, respectively. In each subfigure, the vertical axis's scales of the upper and lower portions are set differently for better visualization and the margin line is highlighted by its value in the blue color.

and a subimage of Pavia city center dataset<sup>3</sup> (of size 200 rows  $\times$  200 columns  $\times$  80 bands) were adopted as the test data. Meanwhile, the same as [3], the spectral vectors in the two datasets were projected on an 8-D signal subspace learned via SVD, in which the bulk of the signal energy is preserved and the noise is largely reduced. These subimages of high quality are considered as the clean HSIs. Two noisy datasets were generated as follows.

**Case 1: Gaussian noise and impulsive noise.**

**Case 2: Gaussian noise and stripes.**

**Case 3: Gaussian noise, impulsive noise, and stripes.**

**Case 4: Poissonian noise, impulsive noise, and stripes.**

In each case:

- 1) the **Gaussian** noise  $\mathbf{n}_i \sim \mathcal{N}(\mathbf{0}, \mathbf{D}^2)$ , where  $\mathbf{D}^2$  is a diagonal matrix with diagonal elements  $\sigma_{i,\text{GT}}^2$

( $i = 1, 2, \dots, b$ ), sampled from a Uniform distribution  $U(0.05, 1)$ .

- 2) the **Poissonian** noise  $\mathbf{Y} \sim \mathcal{P}(\alpha \mathbf{A})$ , where  $\mathcal{P}(\mathbf{A})$  stands for a matrix of size( $\mathbf{A}$ ) of independent Poisson random variables whose parameters are given by the corresponding element of  $\mathbf{A} := [a_{ij}]$ . The parameter  $\alpha$  is such that  $\text{SNR} := \alpha (\sum_{i,j} a_{ij}^2) / (\sum_{i,j} a_{ij})$  was set 10 dB in DCmall data (15 dB in Pavia city center data).
- 3) the **impulsive** noise (salt and pepper) is added to all bands of the HSI and affects 10% pixels in DCmall data (5% pixels in Pavia city center data).
- 4) the **stripes** with different shapes (i.e., vertical lines, oblique lines, curves) affect 60 bands in DCmall data (20 bands in Pavia city center data).

<sup>3</sup>Pavia scenes were provided by Prof. Paolo Gamba from the Telecommunications and Remote Sensing Laboratory, Pavia University (Italy) and can be downloaded from [http://www.ieu.es/crwintco/index.php?title=Hyperspectral\\_Remote\\_Sensing\\_Scenes](http://www.ieu.es/crwintco/index.php?title=Hyperspectral_Remote_Sensing_Scenes)

The parameters of competing methods were set as follows: We used the default parameters for BM4D and TDL. For SSTV, we set  $\lambda = 0.1$ ,  $\mu = 3$ , and  $\nu = 0.2$ . The low-rank regularize parameter  $\tau$  in LRTF-DFR was hand-tuned to obtain optimal results. We used the default block size ( $20 \times 20 \times b$ ) and the step size (4) in LRMR and manually tuned  $r = 5$ .

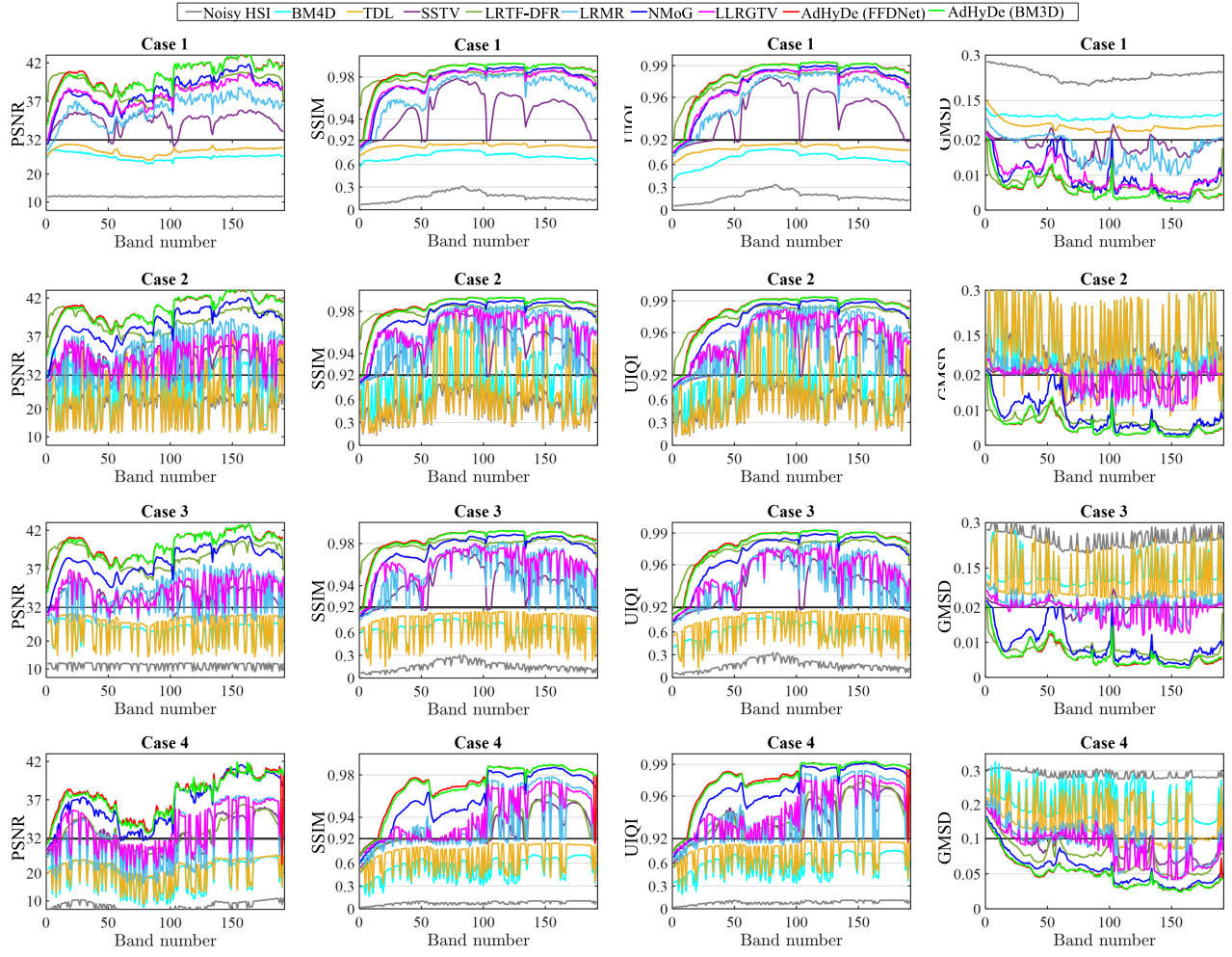


Fig. 2. PSNR, SSIM, UIQI, and GMSD values of each band in the experiment with the Washington dc Mall dataset in different noise cases, respectively. In each subfigure, the vertical axis's scales of the upper and lower portions are set differently for better visualization and the margin line is highlighted by its value in the blue color.

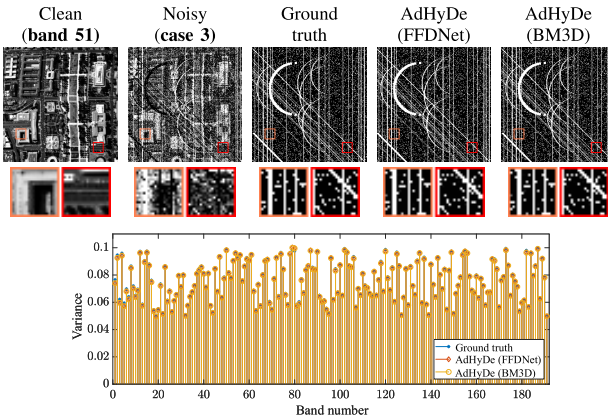


Fig. 3. First row from left to right, respectively, lies the clean image, the noisy image, the ground truth weights, and the estimated weights by our approach with BM3D and FFDNet, in the 51-st band of the Washington dc data with synthetic noise in case 3. The second row presents the values of the  $\sigma_{GT}^2$ s and the estimated  $\sigma_{i,1}^2$ s by the proposed method with BM3D and FFDNet, respectively.

For NMoG, we only tuned the parameter  $r = 3$  for the Pavia city center datasets and used the default values otherwise. The parameters of LLRGTV were manually tuned

as  $\lambda = 0.05$ ,  $\tau = 0.001$ , and  $r = 3$  when dealing with the Pavia center dataset and  $\lambda = 0.15$ ,  $\tau = 0.005$ , and  $r = 5$  for the Washington dc datasets. As for our method, the  $\mu$  and  $\lambda$  were both set as 180 throughout the experiments on the synthetic data, and the dimension of the subspace is set as 3 for the Pavia City Center and 5 for the Washington dc.

The peak signal-to-noise (PSNR) index, the structural similarity index (SSIM) [77], the universal image quality index (UIQI) [78], the spectral angle distance (SAD), and the gradient magnitude similarity deviation (GMSD) index [79] were calculated to give a comprehensive quantitative assessment of the results achieved by the different methods. For the PSNR, SSIM, and UIQI, the larger values indicate the better denoising results while smaller values imply better denoised images for SAD and GMSD. The corresponding mean values of the results obtained by different denoising methods with the simulated noise in different cases for the Pavia city center image and the Washington dc Mall image are reported in Table I, where the best results for each quality index are highlighted in red color, and the second best results are in blue color. In Table I, the proposed AdHyDe with different embedded

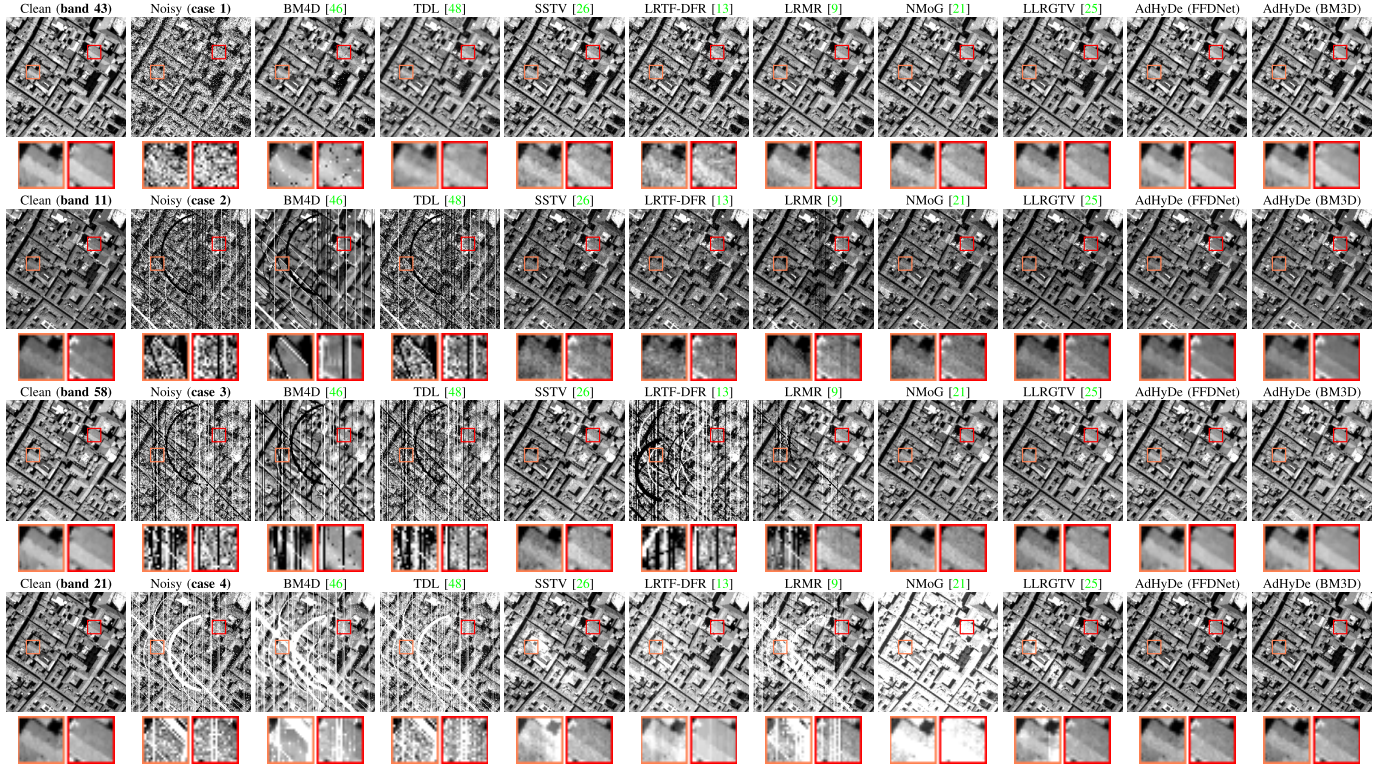


Fig. 4. Denoising result of different bands for Pavia City Center data with different kinds of noise.



Fig. 5. Denoising result of different bands for Washington dc data with different kinds of noise.

denoisers (BM3D and FFDNet) outperformed the other state-of-the-art methods, obtaining the first and the second best results when dealing with different types of mixed noise.

Meanwhile, benefiting from the implementation on the GPU device, the running time of our algorithm with FFDNet is the shortest.

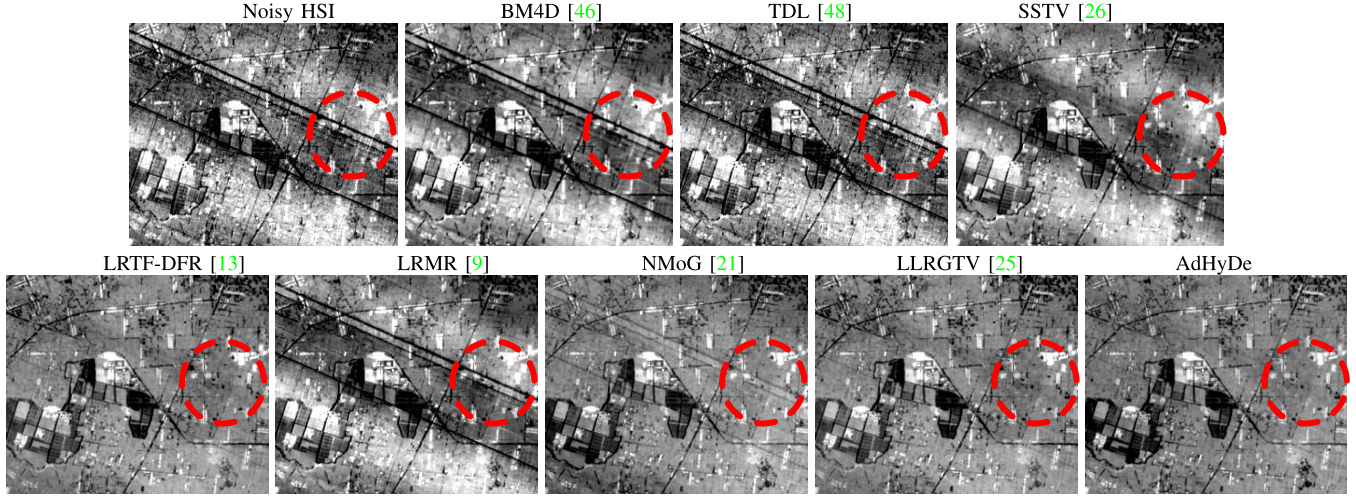


Fig. 6. 35th band of the noisy Tiangong dataset and the denoising results by different methods, respectively.

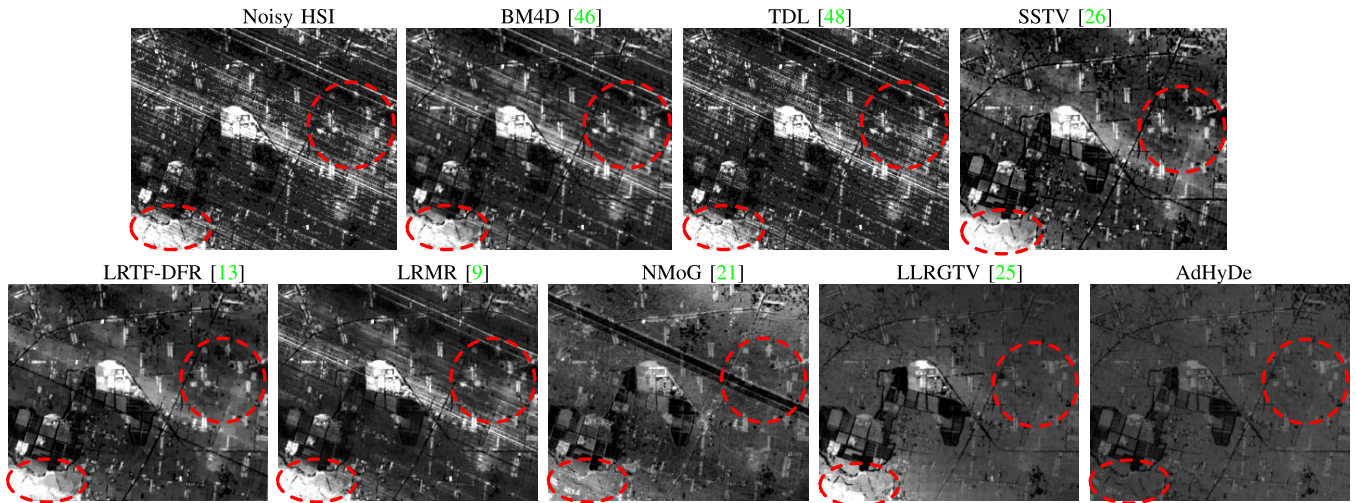


Fig. 7. 36th (bottom ones) band of the noisy Tiangong dataset and the denoising results by different methods, respectively.

To further illustrate these numerical indices, we plot them w.r.t. the band numbers in Figs. 1 and 2. From the figures, the superiority of our method with different denoisers is obvious and the results obtained by our AdHyDe with the FFDNet denoiser (the red lines) and with the BM3D denoiser (the green line) alternatively lead the first place, which verifies the robustness of the proposed algorithm over entire HSI bands with different denoisers.

Figs. 4 and 5 exhibit the restoration results of the Pavia city center and the Washington dc HSIs, respectively. It can be observed that the mixed noise are severe and the competing methods BM4D and TDL can hardly remove this complex mixture noise. We can also see that the performance of LRMR, which is based on the robust principal component analysis, is limited when the components of the noise maintain strong structural features. SSTV, LRTF-DFR, NMoG, and LLRGTV obtain promising results considering the impulsive noise and the stripe noise removal. From the zoomed in red boxes, we can conclude that our method provides the optimum visual quality since it not only removes the impulsive and

stripe noise well but also completely eliminates the Gaussian noise.

In our method, besides the denoising stage, two procedures, i.e., estimating  $\omega_{ij,k}^t$  s in the E-Step and calculating the  $\sigma_{i,1}^2$  s in the M-Step, are of great importance. Thereinto,  $\omega_{ij,k}^t$  is the weight associated with the mixability of the Gaussian noise or the stripe&impulsive noise in the  $i$ th band of the  $j$ th pixel, and  $\sigma_{i,1}^2$  indicates the estimated variance of the Gaussian noise in the  $i$ th band. In the first row of Fig. 3, we display the estimated  $\omega_{ij,2}^t$  s, in which larger values are relevant to greater possibilities of being affected by the stripe&impulsive noise, and the ground truth of mixture degree, in which 1 denotes being affected by stripe&impulsive noise and 0 otherwise, in the 51-st band with synthetic noise in case 3. We can find that our method with different denoisers accurately estimated the mixability except for few pixels. We also plot the estimated  $\sigma_{i,1}^2$  s and the ground truth  $\sigma_{GT}^2$  s in the second row. The desirable fitting of  $\sigma_{i,1}^2$  s and  $\sigma_{GT}^2$  s shows that the proposed method well estimated the bandwisely different variances of the Gaussian noise.

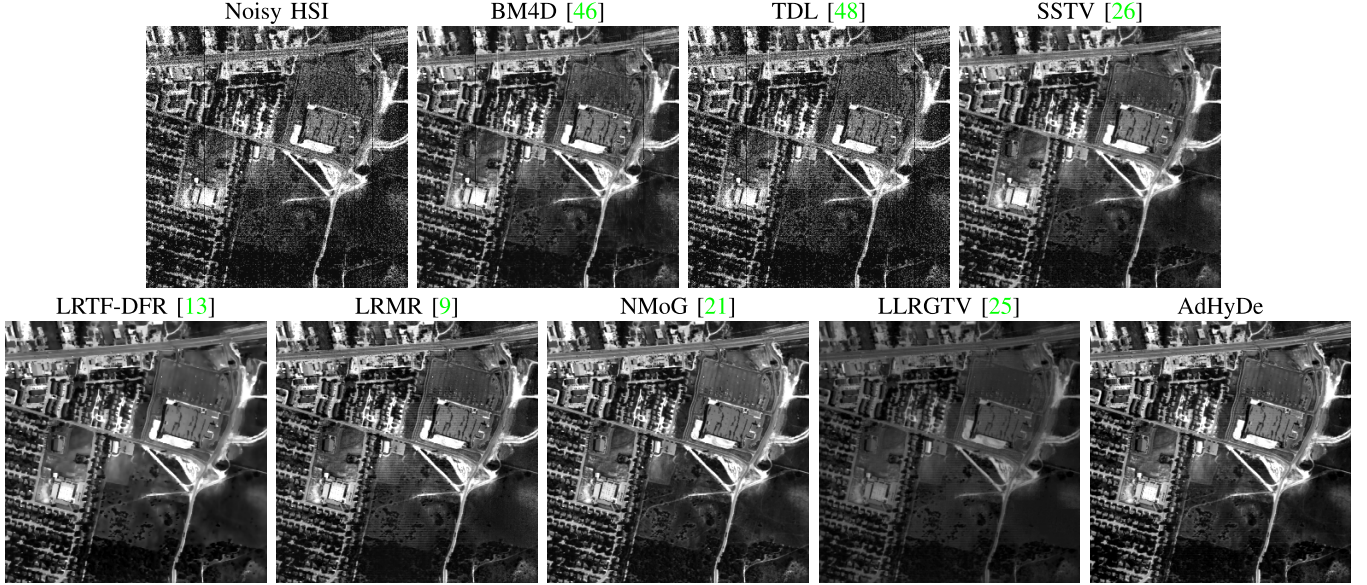


Fig. 8. 240th noisy band of the HYDICE Urban dataset and the denoised results by different methods, respectively.

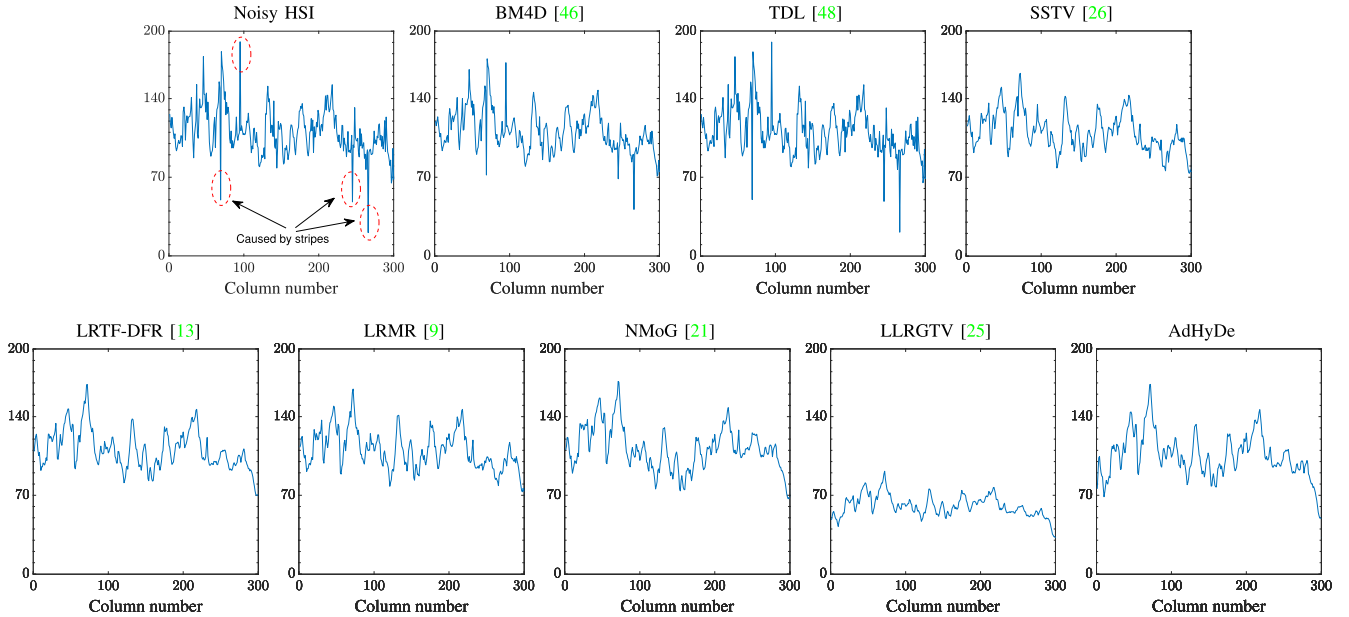


Fig. 9. Vertical mean profiles of band 240 in the HYDICE Urban dataset experiment. From left to right are corresponding to the original data and the denoised results by different methods, respectively. In each subimage, the vertical axis represents the mean value of each column.

It is worth noting that, in this section, our method with different denoisers, i.e., the BM3D and the FFDNet, obtained the comparative results. Actually, we can plug other state-of-the-art denoisers which are made for the natural gray-level images. We have reason to believe that they would also obtain comparative results within our algorithm. For example, in [5], Zhuang *et al.* validated the case of LRCF denoiser [37].

#### B. Evaluation With Real Data

In this section, if not specified, we only use the FFDNet denoiser due to its efficiency. We evaluate the performance of the proposed method on two real HSI datasets:

- 1) Tiangong dataset: The Tiangong dataset was acquired by the Tiangong-1 hyperspectral imager, which is a

128-band push broom scanner with nominal bandwidths of 10 nm visible near-infrared (VNIR) and 23 nm short wave infrared (SWIR), covering a spectral range of 400–2500 nm. In this part, a subset (of size  $240 \times 288 \times 66$ ) was selected.

- 2) HYDICE Urban Dataset: The HYDICE Urban dataset was adopted in the third real data experiment. The original image is  $307 \times 307 \times 210$  in size, and we selected a subimage of  $300 \times 300 \times 210$  for our experiment.

Figs. 6 and 7, respectively, display the images of bands 35 and 36 before and after denoising. In Fig. 6, it can be found that the 35th band is affected by the stripes and sparse noise. LRTF-DFR, NMoG, LLRGTV, and the proposed

AdHyDe removed the stripes and the sparse noise well. The proposed AdHyDe removed the stripes more thoroughly while there remained some distortion in the results by other methods, especially the areas circled the red dashed line. Fig. 7 illustrates that the 36th band is seriously corrupted by various degradations. Our AdHyDe obtained the visually best result considering the restoration of the areas in the red dashline circles.

Figs. 8 and 9 exhibit the denoising results obtained with the HYDICE Urban dataset of band 240 and the corresponding vertical mean profiles, respectively. The band 240 is heavily contaminated by mixed noise, including stripes, impulse and Gaussian noise. As presented in Fig. 8, LRTF-DFR, LRMR, NMoG, and AdHyDe achieved good restoration results while obvious stripes remained within the results by other methods. These remaining stripes resulted in rapid fluctuations in the curves in Fig. 9, which were supposed to be smooth.

#### IV. CONCLUSION

This article introduces a new HSI denoising tailored to mixtures of Gaussian noise, impulsive noise, and stripe noise. On the one hand, the proposed method simultaneously exploits two intrinsic characteristics of HSIs, i.e., the high correlation along the spectral mode and the nonlocal similarity along the spatial modes. On the other hand, an MoG is used to model the mixed noise and the distribution of different types of noise is estimated including their locations. In this sense, the proposed framework automatically adapts to the noise statistics. A comprehensive comparison of the proposed method with the state-of-the-art algorithms was conducted. The results on the simulated and real data show the superiority of the proposed method for complex noise.

#### REFERENCES

- [1] J. M. Bioucas-Dias *et al.*, “Hyperspectral unmixing overview: Geometrical, statistical, and sparse regression-based approaches,” *IEEE J. Sel. Topics Appl. Earth Observ. Remote Sens.*, vol. 5, no. 2, pp. 354–379, Apr. 2012.
- [2] J. M. Bioucas-Dias, A. Plaza, G. Camps-Valls, P. Scheunders, N. Nasrabadi, and J. Chanussot, “Hyperspectral remote sensing data analysis and future challenges,” *IEEE Geosci. Remote Sens. Mag.*, vol. 1, no. 2, pp. 6–36, Jun. 2013.
- [3] L. Zhuang and J. M. Bioucas-Dias, “Fast hyperspectral image denoising and inpainting based on low-rank and sparse representations,” *IEEE J. Sel. Topics Appl. Earth Observ. Remote Sens.*, vol. 11, no. 3, pp. 730–742, Mar. 2018.
- [4] L. Zhuang, L. Gao, B. Zhang, X. Fu, and J. M. Bioucas-Dias, “Hyperspectral image denoising and anomaly detection based on low-rank and sparse representations,” *IEEE Trans. Geosci. Remote Sens.*, early access, Dec. 9, 2020, doi: [10.1109/TGRS.2020.3040221](https://doi.org/10.1109/TGRS.2020.3040221).
- [5] L. Zhuang, X. Fu, M. K. Ng, and J. M. Bioucas-Dias, “Hyperspectral image denoising based on global and nonlocal low-rank factorizations,” *IEEE Trans. Geosci. Remote Sens.*, early access, Jan. 8, 2021, doi: [10.1109/TGRS.2020.3046038](https://doi.org/10.1109/TGRS.2020.3046038).
- [6] M. Simões, J. Bioucas-Dias, L. B. Almeida, and J. Chanussot, “A convex formulation for hyperspectral image superresolution via subspace-based regularization,” *IEEE Trans. Geosci. Remote Sens.*, vol. 53, no. 6, pp. 3373–3388, Jun. 2015.
- [7] L. Gao, D. Yao, Q. Li, L. Zhuang, B. Zhang, and J. Bioucas-Dias, “A new low-rank representation based hyperspectral image denoising method for mineral mapping,” *Remote Sens.*, vol. 9, no. 11, p. 1145, Nov. 2017.
- [8] W. He *et al.*, “Non-local meets global: An integrated paradigm for hyperspectral image restoration,” *IEEE Trans. Pattern Anal. Mach. Intell.*, early access, Sep. 29, 2020, doi: [10.1109/TPAMI.2020.3027563](https://doi.org/10.1109/TPAMI.2020.3027563).
- [9] H. Zhang, W. He, L. Zhang, H. Shen, and Q. Yuan, “Hyperspectral image restoration using low-rank matrix recovery,” *IEEE Trans. Geosci. Remote Sens.*, vol. 52, no. 8, pp. 4729–4743, Aug. 2014.
- [10] Y.-Q. Zhao and J. Yang, “Hyperspectral image denoising via sparse representation and low-rank constraint,” *IEEE Trans. Geosci. Remote Sens.*, vol. 53, no. 1, pp. 296–308, Jan. 2015.
- [11] W. He, H. Zhang, L. Zhang, and H. Shen, “Hyperspectral image denoising via noise-adjusted iterative low-rank matrix approximation,” *IEEE J. Sel. Topics Appl. Earth Observ. Remote Sens.*, vol. 8, no. 6, pp. 3050–3061, Jun. 2015.
- [12] Z. Wu, Q. Wang, J. Jin, and Y. Shen, “Structure tensor total variation-regularized weighted nuclear norm minimization for hyperspectral image mixed denoising,” *Signal Process.*, vol. 131, pp. 202–219, Feb. 2017.
- [13] Y.-B. Zheng, T.-Z. Huang, X.-L. Zhao, Y. Chen, and W. He, “Double-factor-regularized low-rank tensor factorization for mixed noise removal in hyperspectral image,” *IEEE Trans. Geosci. Remote Sens.*, vol. 58, no. 12, pp. 8450–8464, Dec. 2020.
- [14] H. Fan, Y. Chen, Y. Guo, H. Zhang, and G. Kuang, “Hyperspectral image restoration using low-rank tensor recovery,” *IEEE J. Sel. Topics Appl. Earth Observ. Remote Sens.*, vol. 10, no. 10, pp. 4589–4604, Oct. 2017.
- [15] Y. Xie, Y. Qu, D. Tao, W. Wu, Q. Yuan, and W. Zhang, “Hyperspectral image restoration via iteratively regularized weighted schatten  $p$ -norm minimization,” *IEEE Trans. Geosci. Remote Sens.*, vol. 54, no. 8, pp. 4642–4659, Aug. 2016.
- [16] T.-X. Jiang, M. K. Ng, X.-L. Zhao, and T.-Z. Huang, “Framelet representation of tensor nuclear norm for third-order tensor completion,” *IEEE Trans. Image Process.*, vol. 29, pp. 7233–7244, Jun. 2020.
- [17] Y. Chen, Y. Guo, Y. Wang, D. Wang, C. Peng, and G. He, “Denoising of hyperspectral images using nonconvex low rank matrix approximation,” *IEEE Trans. Geosci. Remote Sens.*, vol. 55, no. 9, pp. 5366–5380, Sep. 2017.
- [18] M. Ye, Y. Qian, and J. Zhou, “Multitask sparse nonnegative matrix factorization for joint spectral–spatial hyperspectral imagery denoising,” *IEEE Trans. Geosci. Remote Sens.*, vol. 53, no. 5, pp. 2621–2639, May 2015.
- [19] W. He, H. Zhang, L. Zhang, and H. Shen, “Total-variation-regularized low-rank matrix factorization for hyperspectral image restoration,” *IEEE Trans. Geosci. Remote Sens.*, vol. 54, no. 1, pp. 178–188, Jan. 2016.
- [20] T.-X. Jiang, T.-Z. Huang, X.-L. Zhao, T.-Y. Ji, and L.-J. Deng, “Matrix factorization for low-rank tensor completion using framelet prior,” *Inf. Sci.*, vols. 436–437, pp. 403–417, Apr. 2018.
- [21] Y. Chen, X. Cao, Q. Zhao, D. Meng, and Z. Xu, “Denoising hyperspectral image with non-i.i.d. noise structure,” *IEEE Trans. Cybern.*, vol. 48, no. 3, pp. 1054–1066, Mar. 2018.
- [22] Y. Wang, J. Peng, Q. Zhao, Y. Leung, X.-L. Zhao, and D. Meng, “Hyperspectral image restoration via total variation regularized low-rank tensor decomposition,” *IEEE J. Sel. Topics Appl. Earth Observ. Remote Sens.*, vol. 11, no. 4, pp. 1227–1243, Apr. 2018.
- [23] Y. Chen, W. He, N. Yokoya, T.-Z. Huang, and X.-L. Zhao, “Nonlocal tensor-ring decomposition for hyperspectral image denoising,” *IEEE Trans. Geosci. Remote Sens.*, vol. 58, no. 2, pp. 1348–1362, Feb. 2020.
- [24] H. Zhang, J. Cai, W. He, H. Shen, and L. Zhang, “Double low-rank matrix decomposition for hyperspectral image denoising and destriping,” *IEEE Trans. Geosci. Remote Sens.*, early access, Mar. 10, 2021, doi: [10.1109/TGRS.2021.3061148](https://doi.org/10.1109/TGRS.2021.3061148).
- [25] F. Yang, X. Chen, and L. Chai, “Hyperspectral image destriping and denoising using stripe and spectral low-rank matrix recovery and global spatial-spectral total variation,” *Remote Sens.*, vol. 13, no. 4, p. 827, Feb. 2021.
- [26] H. K. Aggarwal and A. Majumdar, “Hyperspectral image denoising using spatio-spectral total variation,” *IEEE Geosci. Remote Sens. Lett.*, vol. 13, no. 3, pp. 442–446, Mar. 2016.
- [27] Y. Chang, L. Yan, T. Wu, and S. Zhong, “Remote sensing image stripe noise removal: From image decomposition perspective,” *IEEE Trans. Geosci. Remote Sens.*, vol. 54, no. 12, pp. 7018–7031, Dec. 2016.
- [28] Q. Zhang, Q. Yuan, C. Zeng, X. Li, and Y. Wei, “Missing data reconstruction in remote sensing image with a unified spatial-temporal-spectral deep convolutional neural network,” *IEEE Trans. Geosci. Remote Sens.*, vol. 56, no. 8, pp. 4274–4288, Aug. 2018.
- [29] Y. Chang, L. Yan, X.-L. Zhao, H. Fang, Z. Zhang, and S. Zhong, “Weighted low-rank tensor recovery for hyperspectral image restoration,” *IEEE Trans. Cybern.*, vol. 50, no. 11, pp. 4558–4572, Nov. 2020.
- [30] Q. Xie, Q. Zhao, D. Meng, and Z. Xu, “Kronecker-basis-representation based tensor sparsity and its applications to tensor recovery,” *IEEE Trans. Pattern Anal. Mach. Intell.*, vol. 40, no. 8, pp. 1888–1902, Aug. 2018.

- [31] H. Zhang, L. Liu, W. He, and L. Zhang, "Hyperspectral image denoising with total variation regularization and nonlocal low-rank tensor decomposition," *IEEE Trans. Geosci. Remote Sens.*, vol. 58, no. 5, pp. 3071–3084, May 2020.
- [32] Y. Chen, T.-Z. Huang, W. He, N. Yokoya, and X.-L. Zhao, "Hyper-spectral image compressive sensing reconstruction using subspace-based nonlocal tensor ring decomposition," *IEEE Trans. Image Process.*, vol. 29, pp. 6813–6828, May 2020.
- [33] J. Li, J. M. Bioucas-Dias, A. Plaza, and L. Liu, "Robust collaborative nonnegative matrix factorization for hyperspectral unmixing," *IEEE Trans. Geosci. Remote Sens.*, vol. 54, no. 10, pp. 6076–6090, Oct. 2016.
- [34] A. Buades, B. Coll, and J.-M. Morel, "A non-local algorithm for image denoising," in *Proc. IEEE Comput. Soc. Conf. Comput. Vis. Pattern Recognit. (CVPR)*, vol. 2, Jun. 2005, pp. 60–65.
- [35] K. Dabov, A. Foi, V. Katkovnik, and K. Egiazarian, "Image denoising by sparse 3-D transform-domain collaborative filtering," *IEEE Trans. Image Process.*, vol. 16, no. 8, pp. 2080–2095, Aug. 2007.
- [36] W. Dong, L. Zhang, G. Shi, and X. Li, "Nonlocally centralized sparse representation for image restoration," *IEEE Trans. Image Process.*, vol. 22, no. 4, pp. 1620–1630, Apr. 2013.
- [37] M. Nejati, S. Samavi, S. M. R. Soroushmehr, and K. Najarian, "Low-rank regularized collaborative filtering for image denoising," in *Proc. IEEE Int. Conf. Image Process. (ICIP)*, Sep. 2015, pp. 730–734.
- [38] D. Zoran and Y. Weiss, "From learning models of natural image patches to whole image restoration," in *Proc. Int. Conf. Comput. Vis. (ICCV)*, Nov. 2011, pp. 479–486.
- [39] A. Teodoro, M. Almeida, and M. Figueiredo, "Single-frame image denoising and inpainting using Gaussian mixtures," in *Proc. Int. Conf. Pattern Recognit. Appl. Methods (ICPRAM)*, 2015, pp. 283–288.
- [40] S. Gu, Q. Xie, D. Meng, W. Zuo, X. Feng, and L. Zhang, "Weighted nuclear norm minimization and its applications to low level vision," *Int. J. Comput. Vis.*, vol. 121, no. 2, pp. 183–208, Jan. 2017.
- [41] K. Dabov, A. Foi, V. Katkovnik, and K. Egiazarian, "Color image denoising via sparse 3D collaborative filtering with grouping constraint in luminance-chrominance space," in *Proc. IEEE Int. Conf. Image Process.*, vol. 1, Sep. 2007, p. I-313.
- [42] J. Xu, L. Zhang, D. Zhang, and X. Feng, "Multi-channel weighted nuclear norm minimization for real color image denoising," in *Proc. IEEE Int. Conf. Comput. Vis. (ICCV)*, Oct. 2017, pp. 1096–1104.
- [43] J. Xu, L. Zhang, and D. Zhang, "External prior guided internal prior learning for real-world noisy image denoising," *IEEE Trans. Image Process.*, vol. 27, no. 6, pp. 2996–3010, Jun. 2018.
- [44] L. Zhu, C.-W. Fu, M. S. Brown, and P.-A. Heng, "A non-local low-rank framework for ultrasound speckle reduction," in *Proc. IEEE Conf. Comput. Vis. Pattern Recognit. (CVPR)*, Jul. 2017, pp. 5650–5658.
- [45] M. Maggioni, V. Katkovnik, K. Egiazarian, and A. Foi, "Nonlocal transform-domain filter for volumetric data denoising and reconstruction," *IEEE Trans. Image Process.*, vol. 22, no. 1, pp. 119–133, Jan. 2013.
- [46] M. Maggioni, G. Boracchi, A. Foi, and K. Egiazarian, "Video denoising, deblocking, and enhancement through separable 4-D nonlocal spatiotemporal transforms," *IEEE Trans. Image Process.*, vol. 21, no. 9, pp. 3952–3966, Sep. 2012.
- [47] A. Danielyan, A. Foi, V. Katkovnik, and K. Egiazarian, "Denoising of multispectral images via nonlocal groupwise spectrum-PCA," in *Proc. Conf. Colour Graph., Imag., Vis.*, 2010, pp. 261–266.
- [48] Y. Peng, D. Meng, Z. Xu, C. Gao, Y. Yang, and B. Zhang, "Decomposable nonlocal tensor dictionary learning for multispectral image denoising," in *Proc. IEEE Conf. Comput. Vis. Pattern Recognit. (CVPR)*, Jun. 2014, pp. 2949–2956.
- [49] X. Mao, C. Shen, and Y.-B. Yang, "Image restoration using very deep convolutional encoder-decoder networks with symmetric skip connections," in *Proc. Adv. Neural Inf. Process. Syst. (NIPS)*, 2016, pp. 2802–2810.
- [50] K. Zhang, W. Zuo, Y. Chen, D. Meng, and L. Zhang, "Beyond a Gaussian denoiser: Residual learning of deep CNN for image denoising," *IEEE Trans. Image Process.*, vol. 26, no. 7, pp. 3142–3155, Jul. 2017.
- [51] W. Bae, J. Yoo, and J. C. Ye, "Beyond deep residual learning for image restoration: Persistent homology-guided manifold simplification," in *Proc. IEEE Conf. Comput. Vis. Pattern Recognit. Workshops (CVPRW)*, Jul. 2017, pp. 145–153.
- [52] D. Liu, B. Wen, X. Liu, Z. Wang, and T. S. Huang, "When image denoising meets high-level vision tasks: A deep learning approach," 2017, *arXiv:1706.04284*. [Online]. Available: <http://arxiv.org/abs/1706.04284>
- [53] K. Zhang, W. Zuo, and L. Zhang, "FFDNet: Toward a fast and flexible solution for CNN-based image denoising," *IEEE Trans. Image Process.*, vol. 27, no. 9, pp. 4608–4622, Sep. 2018.
- [54] W. Dong, P. Wang, W. Yin, G. Shi, F. Wu, and X. Lu, "Denoising prior driven deep neural network for image restoration," *IEEE Trans. Pattern Anal. Mach. Intell.*, vol. 41, no. 10, pp. 2305–2318, Oct. 2019.
- [55] Q. Yuan, Q. Zhang, J. Li, H. Shen, and L. Zhang, "Hyperspectral image denoising employing a spatial-spectral deep residual convolutional neural network," *IEEE Trans. Geosci. Remote Sens.*, vol. 57, no. 2, pp. 1205–1218, Feb. 2019.
- [56] Q. Zhang, Q. Yuan, J. Li, F. Sun, and L. Zhang, "Deep spatio-spectral Bayesian posterior for hyperspectral image non-i.i.d. noise removal," *ISPRS J. Photogramm. Remote Sens.*, vol. 164, pp. 125–137, Jun. 2020.
- [57] Q. Zhang, Q. Yuan, J. Li, X. Liu, H. Shen, and L. Zhang, "Hybrid noise removal in hyperspectral imagery with a spatial-spectral gradient network," *IEEE Trans. Geosci. Remote Sens.*, vol. 57, no. 10, pp. 7317–7329, Oct. 2019.
- [58] C. Cruz, A. Foi, V. Katkovnik, and K. Egiazarian, "Nonlocality-reinforced convolutional neural networks for image denoising," *IEEE Signal Process. Lett.*, vol. 25, no. 8, pp. 1216–1220, Aug. 2018.
- [59] S. Lefkimiatis, "Non-local color image denoising with convolutional neural networks," in *Proc. IEEE Conf. Comput. Vis. Pattern Recognit. (CVPR)*, Jul. 2017, pp. 5882–5891.
- [60] B. Ahn and N. I. Cho, "Block-matching convolutional neural network for image denoising," 2017, *arXiv:1704.00524*. [Online]. Available: <http://arxiv.org/abs/1704.00524>
- [61] J. M. Bioucas-Dias and J. M. P. Nascimento, "Hyperspectral subspace identification," *IEEE Trans. Geosci. Remote Sens.*, vol. 46, no. 8, pp. 2435–2445, Aug. 2008.
- [62] S. V. Venkatakrishnan, C. A. Bouman, and B. Wohlberg, "Plug-and-play priors for model based reconstruction," in *Proc. IEEE Global Conf. Signal Inf. Process.*, Dec. 2013, pp. 945–948.
- [63] A. Teodoro, J. Bioucas-Dias, and M. Figueiredo, "Sharpening hyperspectral images using plug-and-play priors," in *Proc. Int. Conf. Latent Variable Anal. Signal Separat.* Cham, Switzerland: Springer, 2017, pp. 392–402.
- [64] R. Dian, S. Li, and X. Kang, "Regularizing hyperspectral and multispectral image fusion by CNN denoiser," *IEEE Trans. Neural Netw. Learn. Syst.*, vol. 32, no. 3, pp. 1124–1135, Mar. 2021.
- [65] N. Acito, M. Diani, and G. Corsini, "Signal-dependent noise modeling and model parameter estimation in hyperspectral images," *IEEE Trans. Geosci. Remote Sens.*, vol. 49, no. 8, pp. 2957–2971, Aug. 2011.
- [66] M. L. Uss, B. Vozel, V. V. Lukin, and K. Chehdi, "Local signal-dependent noise variance estimation from hyperspectral textural images," *IEEE J. Sel. Topics Signal Process.*, vol. 5, no. 3, pp. 469–486, Jun. 2011.
- [67] Y. Qian and M. Ye, "Hyperspectral imagery restoration using nonlocal spectral-spatial structured sparse representation with noise estimation," *IEEE J. Sel. Topics Appl. Earth Observ. Remote Sens.*, vol. 6, no. 2, pp. 499–515, Apr. 2013.
- [68] M. Makitalo and A. Foi, "A closed-form approximation of the exact unbiased inverse of the anscombe variance-stabilizing transformation," *IEEE Trans. Image Process.*, vol. 20, no. 9, pp. 2697–2698, Sep. 2011.
- [69] X. Chen *et al.*, "A generalized model for robust tensor factorization with noise modeling by mixture of Gaussians," *IEEE Trans. Neural Netw. Learn. Syst.*, vol. 29, no. 11, pp. 5380–5393, Nov. 2018.
- [70] T.-X. Jiang, L. Zhuang, T.-Z. Huang, and J. M. Bioucas-Dias, "Adaptive hyperspectral mixed noise removal," in *Proc. IEEE Int. Geosci. Remote Sens. Symp. (IGARSS)*, Jul. 2018, pp. 4035–4038.
- [71] A. P. Dempster, N. M. Laird, and D. B. Rubin, "Maximum likelihood from incomplete data via the EM algorithm," *J. Roy. Stat. Soc. B, Methodol.*, vol. 39, no. 1, pp. 1–38, 1977.
- [72] M. V. Afonso, J. M. Bioucas-Dias, and M. A. T. Figueiredo, "An augmented Lagrangian approach to the constrained optimization formulation of imaging inverse problems," *IEEE Trans. Image Process.*, vol. 20, no. 3, pp. 681–695, Mar. 2011.
- [73] T. Meinhardt, M. Moller, C. Hazirbas, and D. Cremers, "Learning proximal operators: Using denoising networks for regularizing inverse imaging problems," in *Proc. IEEE Conf. Comput. Vis. Pattern Recognit. (CVPR)*, Oct. 2017, pp. 1781–1790.
- [74] P. L. Combettes and V. R. Wajs, "Signal recovery by proximal forward-backward splitting," *Multiscale Model. Simul.*, vol. 4, no. 4, pp. 1168–1200, Jan. 2005.
- [75] A. Vedaldi and K. Lenc, "MatConvNet: Convolutional neural networks for MATLAB," in *Proc. 23rd ACM Int. Conf. Multimedia*, Oct. 2015, pp. 689–692.

- [76] A. M. Teodoro, J. M. Bioucas-Dias, and M. A. T. Figueiredo, "A convergent image fusion algorithm using scene-adapted Gaussian-mixture-based denoising," *IEEE Trans. Image Process.*, vol. 28, no. 1, pp. 451–463, Jan. 2019.
- [77] Z. Wang, A. C. Bovik, H. R. Sheikh, and E. P. Simoncelli, "Image quality assessment: From error visibility to structural similarity," *IEEE Trans. Image Process.*, vol. 13, no. 4, pp. 600–612, Apr. 2004.
- [78] H. S. Prashanth, H. L. Shashidhara, and K. N. B. Murthy, "Image scaling comparison using universal image quality index," in *Proc. Int. Conf. Adv. Comput., Control, Telecommun. Technol.*, Dec. 2009, pp. 859–863.
- [79] W. Xue, L. Zhang, X. Mou, and A. C. Bovik, "Gradient magnitude similarity deviation: A highly efficient perceptual image quality index," *IEEE Trans. Image Process.*, vol. 23, no. 2, pp. 684–695, Feb. 2014.



**Tai-Xiang Jiang** (Member, IEEE) received the Ph.D. degree in mathematics from the University of Electronic Science and Technology of China (UESTC), Chengdu, China, in 2019.

He was a cotraining Ph.D. student with the University of Lisbon supervised by Prof. Jose M. Bioucas-Dias from 2017 to 2018. He was the Research Assistant with the Hong Kong Baptist University supported by Prof. Michael K. Ng in 2019. He is an Associated Professor with the School of Economic Information Engineering, Southwestern University of Finance and Economics, Chengdu. His research interests include sparse and low-rank modeling and tensor decomposition for multidimensional image processing, especially on the low-level inverse problems for multidimensional images. <https://taixiangjiang.github.io/>



**Lina Zhuang** (Member, IEEE) received the bachelor's degree in geographic information system and in economics from South China Normal University, Guangzhou, China, in 2012, the M.S. degree in cartography and geography information system from the Institute of Remote Sensing and Digital Earth, Chinese Academy of Sciences, Beijing, China, in 2015, and the Ph.D. degree in electrical and computer engineering from the Instituto Superior Técnico, Universidade de Lisboa, Lisbon, Portugal, in 2018.

From 2015 to 2018, she was a Marie Curie Early Stage Researcher of Sparse Representations and Compressed Sensing Training Network (SpaRTaN number 607290) with the Instituto de Telecomunicações. SpaRTaN Initial Training Networks (ITN) is funded under the European Union's Seventh Framework Program (FP7-PEOPLE-2013-ITN) call and is part of the Marie Curie Actions-ITN funding scheme. From 2019 to 2021, she was a Research Assistant Professor with Hong Kong Baptist University, Hong Kong. She is a Research Assistant Professor with The University of Hong Kong, Hong Kong. Her research interests include hyperspectral image restoration, superresolution, and compressive sensing.



**Ting-Zhu Huang** received the B.S., M.S., and Ph.D. degrees in computational mathematics from the Department of Mathematics, Xi'an Jiaotong University, Xi'an, China, in 1986, 1992, and 2001, respectively.

He is a Professor with the School of Mathematical Sciences, University of Electronic Science and Technology of China, Chengdu, China. His research interests include scientific computation and applications, numerical algorithms for image processing, numerical linear algebra, preconditioning technologies, and matrix analysis with applications.

Dr. Huang is an Editor of *The Scientific World Journal*, *Advances in Numerical Analysis*, the *Journal of Applied Mathematics*, the *Journal of Pure and Applied Mathematics: Advances in Applied Mathematics*, and the *Journal of Electronic Science and Technology*, China.



**Xi-Le Zhao** received the M.S. and Ph.D. degrees from the University of Electronic Science and Technology of China (UESTC), Chengdu, China, in 2009 and 2012, respectively.

He is a Professor with the School of Mathematical Sciences, UESTC. His main research interests are focused on the models and algorithms of high-dimensional image processing problems.



**José M. Bioucas-Dias** (Fellow, IEEE) received the E.E., M.Sc., Ph.D., and Habilitation degrees in electrical and computer engineering from Instituto Superior Técnico (IST), Universidade Técnica de Lisboa (now Universidade de Lisboa), Lisbon, Portugal, in 1985, 1991, 1995, and 2007, respectively.

Since 1995, he has been with the Department of Electrical and Computer Engineering, IST, where he was a Professor and teaches inverse problems in imaging and electric communications. He was also a Senior Researcher with the Pattern and Image Analysis Group, Instituto de Telecomunicações, which is a private nonprofit research institution. His research interests included inverse problems, signal and image processing, pattern recognition, optimization, and remote sensing. He had introduced scientific contributions in the areas of imaging inverse problems, statistical image processing, optimization, phase estimation, phase unwrapping, and in various imaging applications, such as hyperspectral and radar imaging. He was included in Thomson Reuters' Highly Cited Researchers 2015 and 2018 lists and received the IEEE Geoscience and Remote Sensing Society (GRSS) David Landgrebe Award for 2017.